Isospin-projected antisymmetrized molecular dynamics and its application to [10]B

Morita, Hiroyuki; Kanada-En'Yo, Yoshiko

PTEP

Prog. Theor. Exp. Phys. **2016**, 103D02 (14 pages)
DOI: 10.1093/ptep/ptw144

Isospin-projected antisymmetrized molecular dynamics and its application to ^{10}B

Hiroyuki Morita* and Yoshiko Kanada-En'yo

Department of Physics, Kyoto University, Kyoto 606-8502, Japan
*E-mail: morita.hiroyuki.47a@st.kyoto-u.ac.jp

Received April 25, 2016; Revised July 7, 2016; Accepted September 2, 2016; Published October 26, 2016

To investigate *pn* pair correlations in $N = Z =$ odd nuclei, we develop a new framework based on the generator coordinate method of the $\beta\gamma$ constraint antisymmetrized molecular dynamics. In the framework, the isospin projection is approximately performed before the energy variation to obtain the wave function optimized for each isospin. We apply the method to ^{10}B and show that it works well to describe coexistence of $T = 0$ and $T = 1$ states in low-energy spectra. Structures of low-lying states and *pn* correlations are investigated. Strong $M1(0^+_1 \to 1^+_1)$ and $E2(1^+_1 \to 1^+_2)$ transitions are understood by the spin excitation of the *pn* pair and the rotation of a deformed core, respectively.

Subject Index D11

1. Introduction

Proton and neutron (*pn*) correlation is one of the key phenomena for understanding properties of nuclei along the $N = Z$ line in the nuclear chart (see Ref. [1] and references therein). Unlike in identical pair correlations, two channels, $T = 0$ and $T = 1$, are possible in *pn* pair correlations, and both channels play an important role in various nuclear structures. Competition between $T = 0$ and $T = 1$ *pn* pairs has been attracting great interest and proposed as describing level ordering of $J^\pi T = 1^+0$ and $J^\pi T = 0^+1$ states in $N = Z =$ odd nuclei and neighboring nuclei. In the heavy-mass region, the competition has been investigated with mean-field approaches [2–7]. In the light-mass region, properties of a *pn* pair at the nuclear surface have been studied in detail to understand low-lying spectra of $N = Z =$ odd nuclei [8–10].

As discussed in the study with a three-body model calculation [8], a proton and a neutron around a core nucleus form a *pn* pair in the $T = 0$ or $T = 1$ channel because of the S-wave attraction between nucleons. The $T = 1$ *pn* pair is the mirror state of the dineutron pair, which is often discussed in neutron-rich nuclei. The appearance of the $T = 0$ *pn* pair is peculiar to $N = Z =$ odd nuclei. Unlike the $T = 1$ pair, the $T = 0$ *pn* pair has the finite intrinsic spin $S = 1$ like a deuteron, and therefore it provides different J states in the low-energy region because of angular momentum coupling. Indeed, it is experimentally known that many $T = 0$ states coexist along with the $J^\pi T = 0^+1$ state in low-energy spectra of $N = Z =$ odd nuclei [1]. Moreover, a high J state with $T = 0$ comes down to the ground state in many $N = Z =$ odd nuclei in the light-mass region except for those with closed-shell cores. For example, the ground state spin parity of ^{10}B with $Z = N = 5$ is 3^+, for which the importance of three-nucleon forces is discussed in the no-core shell model calculations [11,12].

In systematic study of general $N = Z =$ odd nuclei, it is important to describe the competition between the $T = 0$ and $T = 1$ *pn* correlations while taking into account spin configurations as well as nuclear deformation. In the light-mass $N = Z$ region, cluster structure is another important feature which brings rich structures together with the *pn* correlations. The *pn* pair feature and its dynamics can be affected by the cluster structure.

To deal with these problems, we developed a new method based on antisymmetrized molecular dynamics (AMD) [13–17] with a constraint on the quadrupole deformation parameters, called $\beta\gamma$ constraint AMD [18,19]. This has been proved to be a useful approach for studying structures of stable and unstable nuclei. In the AMD method, the existence of a core nucleus, a *pn* pair, and a cluster structure are not *a priori* assumed, but degrees of freedom of all nucleons are independently treated in basis wave functions given by Slater determinants of Gaussian wave packets. Nevertheless, if a system favors a structure with a *pn* pair and cluster structures, such a structure is obtained in the energy variation. In the new method, isospin projection is approximately performed before the energy variation to obtain the AMD wave function optimized for each isospin state. We call this method isospin-projected $\beta\gamma$ constraint AMD, $T\beta\gamma$-AMD. Energy levels of $N = Z =$ odd nuclei are calculated with the $T\beta\gamma$-AMD method combined with the generator coordinate method (GCM), called $T\beta\gamma$-AMD+GCM. To test the applicability of the new framework, we apply the method to ^{10}B, in which $2\alpha + pn$ structures are found in low-lying $T = 0$ and $T = 1$ states. We investigate *pn* correlations around the 2α core, and show the importance of the finite spin of the $T = 0$ *pn* pair, which couples with the *pn* motion and the core rotation, in the low-lying states of ^{10}B.

The paper is organized as follows. We explain the framework of $T\beta\gamma$-AMD in Sect. 2, and the adopted effective nuclear interactions in Sect. 3. We show the calculated results of ^{10}B in Sect. 4, and discuss the structures of ^{10}B focusing on the *pn* correlation in Sect. 5. Finally, a summary and an outlook are given in Sect. 6.

2. Framework of $T\beta\gamma$ constraint AMD

Antisymmetrized molecular dynamics is one of the most useful approaches to describe the cluster aspect of light nuclei. However, the conventional AMD method is not sufficient for $N = Z =$ odd nuclei, in which the isospin $T = 0$ and $T = 1$ states degenerate in the low-energy region. In this section, we explain the framework of isospin-projected AMD, which is a newly developed method for the study of $N = Z =$ odd nuclei. We also describe the detailed formulation of the present calculation which is based on the isospin-projected version of $\beta\gamma$ constraint AMD combined with GCM.

2.1. AMD framework

The AMD framework is based on a variational method. An AMD wave function is a Slater determinant of Gaussian wave packets:

$$|\Phi\rangle = \mathcal{A}\,|\phi_1\rangle\,|\phi_2\rangle\cdots|\phi_A\rangle\,, \tag{1}$$

where $\mathcal{A}$ refers to the antisymmetrization operator and ϕ_i refers to the ith single-particle wave function. ϕ_i is expressed by a product of the spatial (ψ_i), spin (ξ_i), and isospin (n_i) parts as

$$|\phi_i\rangle = |\psi_i\rangle\,|\xi_i\rangle\,|n_i\rangle\,, \tag{2}$$

where

$$\langle \boldsymbol{r} | \psi_i \rangle = \left(\frac{2\nu}{\pi}\right)^{\frac{3}{4}} \exp\left[-\nu\left(\boldsymbol{r} - \frac{\boldsymbol{Z}_i}{\sqrt{\nu}}\right)^2 + \frac{1}{2}\boldsymbol{Z}_i^2\right], \tag{3}$$

$$|\xi_i\rangle = \xi_{i\uparrow}|\uparrow\rangle + \xi_{i\downarrow}|\downarrow\rangle, \tag{4}$$

$$|n_i\rangle = |p\rangle \text{ or } |n\rangle. \tag{5}$$

The parameters of Gaussian centroids $\{\boldsymbol{Z}_i\}_{i=1,2,\ldots,A}$ and those of spin orientations $\{\boldsymbol{\xi}_i\}_{i=1,2,\ldots,A}$ are optimized in the energy variation, whereas each isospin configuration is fixed to be an isospin eigenstate as $|p\rangle$ or $|n\rangle$.

In the AMD wave function expressed by a Slater determinant, some symmetries, such as the parity and rotational symmetries, are usually broken. To obtain physical wave functions for energy levels, parity and angular momentum projections are performed to restore the broken symmetries in the AMD framework. In most cases, the parity projection is performed before the energy variation but the angular momentum projection is done after the variation to save computational costs, except for the extended AMD calculation with the variation after the parity and angular momentum projections (AMD+VAP^J) [20]. In other words, energy variation is performed for the AMD wave function projected to the parity eigenstate with the parity projection operator P^π as

$$\delta \frac{\langle \Phi^\pi | H | \Phi^\pi \rangle}{\langle \Phi^\pi | \Phi^\pi \rangle} = 0, \tag{6}$$

$$\left|\Phi^\pi\right\rangle = P^\pi |\Phi\rangle. \tag{7}$$

For numerical calculation of the energy variation we adopt the frictional cooling method, which is a gradient method. After variation, we project the obtained AMD wave functions to the parity and angular momentum eigenstates, and mix the different K states. Expectation values are calculated for the parity and angular momentum projected states with K-mixing.

To describe the ground and excited states, we superpose various AMD wave functions based on GCM with the $\beta\gamma$ constraint AMD method [19], which is an efficient method to choose basis AMD wave functions for a multi-configuration calculation.

In $\beta\gamma$ constraint AMD, the energy variation is performed under a constraint on the quadrupole deformation parameters β and γ. The method has been proved to be useful to describe spatially developed cluster states as well as deformed states. To perform the energy variation with a constraint $\bar{C}[\Phi] = C_i$, we add a penalty term to the energy expectation value:

$$\langle H \rangle \to \langle H \rangle + \eta\left(\bar{C}[\Phi] - C_i\right)^2, \tag{8}$$

where η is a large enough positive value. After the energy variation with the penalty term, we obtain the optimized configuration $\Phi(C_i)$ for the energy minimum state in the AMD model space with the condition $\bar{C}[\Phi] = C_i$.

We superpose the wave functions obtained for different constraint values C_i based on the GCM method with the generator coordinate $\bar{C}[\Phi]$. In $\beta\gamma$ constraint AMD, C_i indicates the set of quadrupole deformation parameters, $C_i = (\beta_i, \gamma_i)$, which specifies the nuclear deformation. Then, the GCM wave function is given by the superposition of the parity and angular momentum projected wave functions

obtained by the $\beta\gamma$ constraint AMD as

$$|\Psi\rangle = \sum_{i=1}^{i_{\max}} \sum_{K=-J}^{J} g_{iK}^{\pi J} P^{\pi} P_{MK}^{J} |\Phi(C_i)\rangle, \tag{9}$$

where K refers to the intrinsic magnetic quantum number and $i_{\max}$ is the number of superposed wavefunctions. The coefficients $\{g_{iK}^{\pi J}\}$ are determined by the diagonalization of the Hamiltonian and norm matrices.

2.2. *Isospin projection*

In $N = Z =$ odd nuclei, isospin projection is necessary to describe different isospin states $T = 0, 1$, which degenerate in a low-energy region. As for parity projection, isospin projection enables us to obtain a better wave function optimized for each isospin. The isospin projection is also important for obtaining proper intrinsic spin structures because the isospin of a *pn* pair restricts the intrinsic spin of the pair because of the Fermi statistics of two nucleons.

In the present calculation of $N = Z$ nuclei, we approximately perform the isospin projection with the following operator:

$$P^T = 1 + \pi^T P_{pn}, \tag{10}$$

where $\pi^T = (-1)^Z, -(-1)^Z$ for $T = 0, 1$ respectively. Here, P_{pn} is the operator which exchanges the isospin, proton $\leftrightarrow$ neutron, of all nucleons in the AMD wave function:

$$P_{pn} |\Phi\rangle = \mathcal{A} |\psi_1\rangle |\xi_1\rangle |-n_1\rangle |\psi_2\rangle |\xi_2\rangle |-n_2\rangle \cdots |\psi_A\rangle |\xi_A\rangle |-n_A\rangle, \tag{11}$$

where $|-p\rangle \equiv |n\rangle$ and $|-n\rangle \equiv |p\rangle$. P^T is a good approximation of the isospin projection operator for an $N = Z =$ odd system having a proton and a neutron with an approximately $T = 0$ core nucleus. Strictly speaking, P^T just distinguishes the $T = 0, 2, 4, \ldots$ states from the $T = 1, 3, 5, \ldots$ states, and it is equivalent to the isospin projection operator only for states with no $T \geq 2$ component. In the present case of ^{10}B, $T \geq 2$ components are minor, as shown later.

2.3. *Isospin-projected AMD*

In the isospin-projected AMD framework, the isospin projection is performed before the energy variation. In the present calculation, the method is used for $\beta\gamma$ constraint AMD. In other words, the energy variation is performed with the β and γ constraints after the isospin and parity projections but before the angular momentum projection as

$$\delta \frac{\langle \Phi^{T\pi} | H | \Phi^{T\pi} \rangle}{\langle \Phi^{T\pi} | \Phi^{T\pi} \rangle} = 0, \tag{12}$$

$$|\Phi^{T\pi}\rangle = P^T P^{\pi} |\Phi\rangle, \tag{13}$$

with the penalty term

$$\langle H \rangle \to \langle H \rangle + \eta \left[\left(\beta_i \cos\gamma_i - \bar{\beta} \cos\bar{\gamma} \right)^2 + \left(\beta_i \sin\gamma_i - \bar{\beta} \sin\bar{\gamma} \right)^2 \right], \tag{14}$$

where $\bar{\beta}$ and $\bar{\gamma}$ are defined as

$$\bar{\beta} \cos\bar{\gamma} = \frac{\sqrt{5\pi}}{3} \frac{2\langle z^2 \rangle - \langle x^2 \rangle - \langle y^2 \rangle}{R^2}, \tag{15}$$

$$\bar{\beta}\sin\bar{\gamma} = \sqrt{\frac{5\pi}{3}}\frac{\langle x^2\rangle - \langle y^2\rangle}{R^2}, \tag{16}$$

$$R^2 = \frac{5}{3}\left(\langle x^2\rangle + \langle y^2\rangle + \langle z^2\rangle\right). \tag{17}$$

We call this method T-projected $\beta\gamma$-constraint AMD ($T\beta\gamma$-AMD). In this method, β and γ are the parameters which control the development of clusters including pn pairs. In the application to the ^{10}B nucleus with $2\alpha + pn$ structures, γ plays the role of the parameter for the spatial development of the pn pair, whereas β is related to the α–α distance, as shown later. After the energy variation, we perform the GCM calculation by superposing the projected AMD wave functions with respect to the discretized generator coordinates β_i and γ_i:

$$|\Psi\rangle = \sum_{i=1}^{i_{\max}}\sum_{K=-J}^{J} g_{iK}^{T\pi J} P^T P^\pi P^J_{MK} \left|\Phi\left(\beta_i\gamma_i\right)\right\rangle. \tag{18}$$

In the present calculation, we omit the isospin mixing in the wave functions. Note that the isospin mixing by the Coulomb force can be taken into account in the present framework by superposing different T states in the GCM calculation. We have checked that the effect of isospin mixing is very small for low-lying states of ^{10}B. (The isospin mixing is $< 0.01\%$ and the energy gain by the isospin mixing is < 30 keV.)

3. Hamiltonian and parameters

The Hamiltonian used in the present work is

$$H = K - K_{\rm cm} + V_{\rm c} + V_{\rm ls} + V_{\rm Coulomb}, \tag{19}$$

where K, $K_{\rm cm}$, $V_{\rm c}$, $V_{\rm ls}$, and $V_{\rm Coulomb}$ are the kinetic energy, kinetic energy of the center of mass, central force, spin–orbit force, and Coulomb force, respectively. The Coulomb force is approximated by a seven-range Gaussian as in Ref. [21]. For the central force and the spin–orbit force, the following effective nuclear forces are adopted as in the previous work [22]. The Volkov No. 2 force [23] is used for $V_{\rm c}$,

$$V_{\rm c} = \sum_{i<j}\sum_{k=1,2} v_k \exp\left[-\left(\frac{\boldsymbol{r}_i - \boldsymbol{r}_j}{a_k}\right)^2\right](W + BP_\sigma - HP_\tau - MP_\sigma P_\tau), \tag{20}$$

where $v_1 = -60.65$ MeV, $v_2 = 61.14$ MeV, $a_1 = 1.80$ fm, and $a_2 = 1.01$ fm. As for the Wigner, Majorana, Bartlett, and Heisenberg parameters, we adopt the same parameters as those used in the previous work [22]: $W = 1 - M = 0.40$, $M = 0.60$, and $B = H = 0.06$. These parameters reproduce the $\alpha\alpha$ scattering phase shift. The Bartlett and Heisenberg parameters were fitted to the relative energy between $T = 0$ and $T = 1$ states of the ^{10}B spectra in the AMD+VAP^J calculation.

For $V_{\rm ls}$, the spin–orbit term of the Gaussian three-range soft-core force (G3RS) [24,25] is used as

$$V_{\rm ls} = \sum_{i<j}\sum_{k=1,2} u_k \exp\left[-\left(\frac{\boldsymbol{r}_i - \boldsymbol{r}_j}{b_k}\right)^2\right]\frac{1+P_\sigma}{2}\frac{1+P_\tau}{2}\boldsymbol{l}_{ij}\cdot\boldsymbol{s}_{ij}, \tag{21}$$

$$\boldsymbol{l}_{ij} = \left(\boldsymbol{r}_i - \boldsymbol{r}_j\right)\times\frac{\boldsymbol{p}_i - \boldsymbol{p}_j}{2}, \tag{22}$$

$$\boldsymbol{s}_{ij} = \boldsymbol{s}_i + \boldsymbol{s}_j, \tag{23}$$

where b_1 =0.60 fm, b_2 =0.447 fm. The strengths used in the present calculation are $u_1 = -u_2$ =1300 MeV, which was fitted to reproduce the ls splitting between $3/2^-$ and $1/2^-$ states in ^{9}Be in the AMD+VAP^J calculation [22].

4. Results

To test the applicability of $T\beta\gamma$-AMD, we apply it to ^{10}B and show the advantages of this method. ^{10}B is an ideal benchmark nucleus for the following reasons. First, ^{10}B is an $N = Z$ nucleus, in which different isospin states appear in its low-energy region. Indeed, $J^\pi T = 3^+0, 1^+0$, and 0^+1 states are known in the low-lying ^{10}B spectra. Second, ^{10}B is considered to have the $2\alpha + pn$ structure. This means that ^{10}B can be a good example of a system having a pn pair around a deformed core. We investigate structures of low-lying $T = 0$ and $T = 1$ states in ^{10}B while focusing on the pn correlation around the 2α core.

4.1. *Energy variation with and without the isospin projection*

In the framework of isospin-projected AMD, we obtain the state optimized for each isospin $T = 0, 1$ because the energy variation is performed for the isospin-projected AMD wave function as explained previously. The variation after the isospin projection (VAP^T) is essential to clarify the nuclear structure along the $N = Z$ line on the nuclear chart because different isospin states have almost the same energy and compete with each other in $N = Z =$ odd nuclei. This is an advantage of $T\beta\gamma$-AMD over the usual $\beta\gamma$-AMD, in which the variation is performed without the isospin projection. In this subsection, we compare the energy surface on the $\beta\gamma$-plane obtained by $T\beta\gamma$-AMD with that of $\beta\gamma$-AMD and show the availability of the variation after the isospin projection in the present framework, $T\beta\gamma$-AMD.

First, we show the energy on the $\beta\gamma$-plane obtained by $T\beta\gamma$-AMD. Figure 1 shows the $T = 0, 1$ $\pi = +$ energy surfaces of ^{10}B obtained by variation after the parity and isospin projections. The minimum point in the $T = 1$ plane [Fig. 1(b)] is located at $(\beta\cos\gamma, \beta\sin\gamma) = (0.4, 0.1)$, and that in the $T = 0$ plane [Fig. 1(a)] is at $(0.38, 0)$. The finite γ value is mainly caused by spatial development of the pn pair, as discussed later.

We also calculate the expectation values of total isospin T^2 on each $\beta\gamma$-plane. The values are $\langle T^2\rangle < 0.070$ for $T = 0$ states and $2 < \langle T^2\rangle < 2.015$ for $T = 1$ states. This means that the operator P^T defined in Eq. (10) successfully works as the isospin projection operator for ^{10}B.

Next, we discuss the results obtained by $\beta\gamma$-AMD, which is a conventional AMD method with parity projection but without the isospin projection. Figure 2(a) shows the $\pi = +$ energy surface of ^{10}B obtained by $\beta\gamma$-AMD. It is notable that there is a gap along the line from (0.2,0.1) to (0.6,0). This is caused by the drastic change of the intrinsic structure from the small-γ region to the relatively large-γ region.

We also calculate the energy expectation values of the $T = 0, 1$ eigenstates projected from the $\beta\gamma$-AMD wave functions obtained by the variation before the isospin projection (VBP^T). The $T = 0$ and $T = 1$ $\pi = +$ energy surfaces of the VBP^T are shown in Figs. 2(b) and (c), respectively. The $T = 0, 1$ energy surfaces of the VBP^T also show the discontinuity along the same line on the $\beta\gamma$-plane originating in the difference in the intrinsic structure in the two regions. The $T = 0$ energy surface in the small-γ region corresponds well to the $T = 0$ result obtained by VAP^T shown in Fig. 1(a), whereas the $T = 1$ energy surface in the large-γ region is similar to the $T = 1$ result of VAP^T in Fig. 1(b). This means that, for the small-γ region, VBP^T gives wave functions almost the

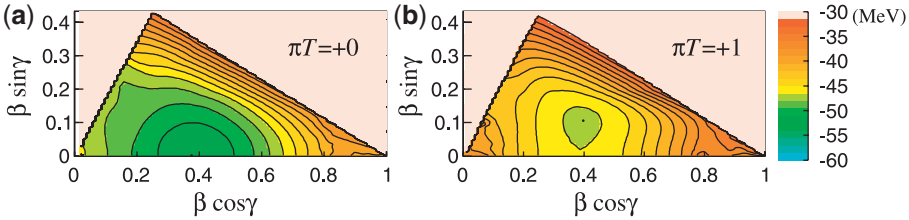

Fig. 1. Energy surfaces on the $\beta\gamma$-plane of ^{10}B obtained by $T\beta\gamma$-AMD. The left (right) panel shows the $T = 0$ ($T = 1$) $\pi = +$ energy surface. The energy minimum of each energy surface is shown by a dot.

same as those optimized for the $T = 0$ component, and for the large-γ region, it produces solutions similar to those optimized for the $T = 1$ component.

In order to clarify how much the wavefunctions obtained by $\beta\gamma$-AMD contain $T = 0$ or 1 components, we calculated the ratio of the norm for the $T = 1$ state to the total norm and we show it in Fig. 3. In the small-γ region the ratios are almost zero, and in the large-γ region they go up to 0.5. This supports the fact that the states obtained without isospin projection have almost no $T = 0$ components in the small-γ region, and they contain comparable $T = 0, 1$ components in the large-γ region.

From these results, it is clear that the VBP^T method is not applicable for obtaining the optimum wave functions on the $\beta\gamma$-plane for each isospin. As seen in Fig. 2(b), VBP^T fails to obtain the $T = 1$ states in the small-γ region, that is, the $T = 1$ wave functions with prolate deformations. As already shown in Fig. 1, the $T = 0$ and $T = 1$ states exist at each point on the $\beta\gamma$-plane. However, in VBP^T, the $T = 0$ and $T = 1$ states cannot be optimized separately, but either of the $T = 0, 1$ states or a mixed state of $T = 0$ and $T = 1$ components is optimized. The discontinuity on the $\beta\gamma$-plane in the VBP^T results can be a crucial problem in describing the γ mode, which is related to *pn* pair motion, and in calculating excited states in each isospin channel. In other words, in the VBP^T results, the parameters β and γ cannot be adopted as generator coordinates in the GCM calculation because basis wave functions in some region on the $\beta\gamma$-plane are missing.

On the other hand, the VAP^T technique enables us to optimize $T = 0$ and $T = 1$ components separately even though they almost degenerate at each constraint point. Consequently, the discontinuity on the $\beta\gamma$-plane disappears and smooth energy surfaces are obtained for each isospin states by $T\beta\gamma$-AMD, as shown in Fig. 1. This is one of the advantages of the present method and important in describing the γ mode for *pn* pair motion in detail.

4.2. *Angular momentum projected energy surfaces and intrinsic structures*

We discuss the angular momentum projected energies of $T\beta\gamma$-AMD, which are calculated by the angular momentum projection of the wave functions obtained by $T\beta\gamma$-AMD. Figure 4 shows the energy surfaces on the $\beta\gamma$-plane for the $J^\pi T = 0^+1$, 3^+0, and 1^+0 states. Here, the K-mixing is taken into account and the lowest energy is shown at each point on the $\beta\gamma$-plane except for Fig. 4(c). The $J^\pi T = 1^+0$ states on the $\beta\gamma$-plane contain two components with different K quanta corresponding to the low-lying $1^+_1 0$ and $1^+_2 0$ states. Figures 4(b) and (c) show the energy surfaces for the first and the second lowest energies obtained by the K-mixing at each point. The 3^+0 energy surface is approximately described by the energy of the $K = 3$ component on the $\beta\gamma$-plane, whereas the $1^+_1 0$ and $1^+_2 0$ energy surfaces are roughly described by the energies of the $K = 1$ and $K = 0$ components, respectively, though strictly speaking the K-mixing occurs for $\gamma \neq 0$ states.

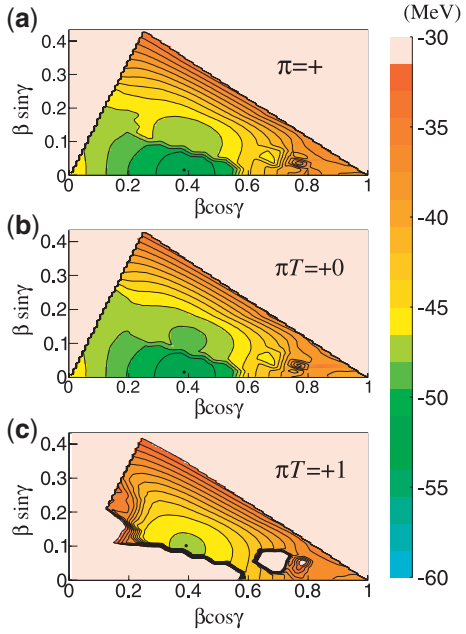

Fig. 2. Energy surfaces on the $\beta\gamma$-plane of ^{10}B obtained by VBP^T. (a) The $\pi = +$ energy surface obtained by $\beta\gamma$-AMD variation without isospin projection. (b, c) The $T = 0$ and $T = 1$ projected $\pi = +$ energy surfaces of VBP^T. The energy minimum of each energy surface is shown by a dot.

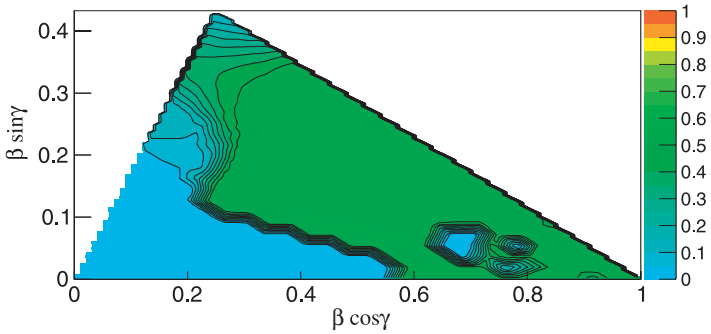

Fig. 3. The ratio of the norm for the $\pi T = +1$ state to that for the $\pi = +$.

Compared with the $T = 0$ and $T = 1$ energy surfaces before the angular momentum projection in Fig. 1, the energy minimum positions are shifted toward larger deformation β regions by the angular momentum projection, meaning that deformed states are more favored after the angular momentum projection. The energy minimum state at $(\beta\cos\gamma, \beta\sin\gamma) = (0.54, 0.12)$ for $\beta = 0.55, \gamma = 12.5°$ on the $J^\pi T = 0^+1$ energy surface [Fig. 4(a)] is the dominant component of the lowest isovector ($T = 1$) state, ^{10}B(0^+_1), and that at $(0.52, 0.08)$ for $\beta = 0.53, \gamma = 8.7°$ on the 3^+0 energy surface [Fig. 4(d)] approximately describes the lowest isoscalar ($T = 0$) state, the ^{10}B ground state ($3^+_1 0$). The energy minimum state at $(0.5, 0.21)$ on the $J^\pi T = 1^+_1 0$ energy surface and that at $(0.29, 0.27)$ on the $J^\pi T = 1^+_2 0$ energy surface approximately correspond to ^{10}B(1^+_1) and ^{10}B(1^+_2), respectively.

Let us discuss intrinsic structures of the states obtained by $T\beta\gamma$-AMD. The AMD wave functions before the projections at the energy minima on the $J^\pi T = 0^+1$, 3^+0, $1^+_1 0$, and $1^+_2 0$ energy surfaces [Fig. 4(a–d)] are regarded as the intrinsic states of the dominant components of the 0^+1, 3^+0, $1^+_1 0$, and $1^+_2 0$ states of ^{10}B. In Fig. 5, we show the intrinsic density distribution of the minimum energy states

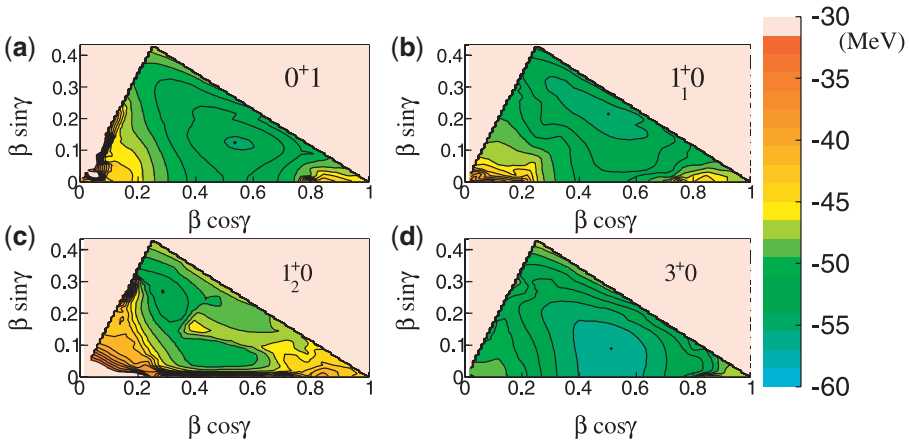

Fig. 4. J^π-projected energy surfaces of VAP^T on the $\beta\gamma$-plane of ^{10}B. Panels (a), (b), (c), and (d) refer to 0^+1, $1^+_1 0$, $1^+_2 0$, and 3^+0, respectively. The energy minimum on each energy surface is shown by a dot.

projected onto the xz-plane by integrating the density along the y-axis, $\rho\,(x,z) = \int \rho\,(x,y,z)\,dy$. The density distribution shows the structure of a 2α core with a pn pair in the low-lying states of ^{10}B. In the 0^+1 state, three $T = 1$ pn pairs with the anti-parallel spin configuration ($S = 0$) are found in the right side forming an α cluster with an $S = 0$ pn pair near the α cluster. In the 3^+0 state, the $T = 0$ ($S = 1$) pn pair is formed but it shows no spatial development because the pn pair is rotating around the 2α core in the $L = 2$ (D-wave) and strongly attracted by the spin–orbit potential from the core. In the $1^+_1 0$ and $1^+_2 0$ states, a $T = 0$ pn pair has the parallel spin configuration indicating the formation of the $T = 0$, $S = 1$ pn pair. The pn pair in the 1^+0 states is farther away from the 2α core compared with those in the 0^+1 and 3^+0 states, indicating remarkable spatial development of the $T = 0$, $S = 1$ pn pair.

From the analysis of intrinsic structures obtained by $T\beta\gamma$-AMD on the $\beta\gamma$-plane, it is found that the $T = 0, S = 1$ ($T = 1, S = 0$) pn pair is formed in the $T = 0$ ($T = 1$) states, and it goes away in the transverse direction from the 2α with increase of γ. In other word, the γ mode on the $\beta\gamma$-plane approximately corresponds to pn pair motion relative to the 2α core.

Let us come back to the energy surfaces shown in Fig. 4. The 0^+1 energy surface shows a plateau from the minimum along the γ parameter up to the $\gamma = 60°$ line, which corresponds to a soft mode of the $T = 1, S = 0$ pn pair motion relative to the 2α core in the $0^+_1 1$ state. The $1^+_1 0$ energy surface shows a more remarkable plateau for the spatial development of the $T = 0, S = 1$ pn pair. In contrast, the 3^+0 energy surface does not show such a plateau toward the $\gamma = 60°$ direction meaning that the pn pair in the $3^+_1 0$ state is deeply bound near the core because of the spin–orbit potential from the core.

4.3. *GCM results*

We superpose $i_{\max} = 91$ wave functions on the $\beta\gamma$-plane for each isospin and calculate energy spectra, moments, and transition strengths. The parity, isospin, and the angular momentum projections with K-mixing are taken into account in the GCM calculation as described in Eq. (18). The generator coordinates, β and γ, effectively describe the pn pair motion relative to the 2α core as well as the α–α motion. Note that we do not show spectra based on $\beta\gamma$-AMD below because in these case β and γ are no longer proper generator coordinates, as we pointed in Sect. 4.

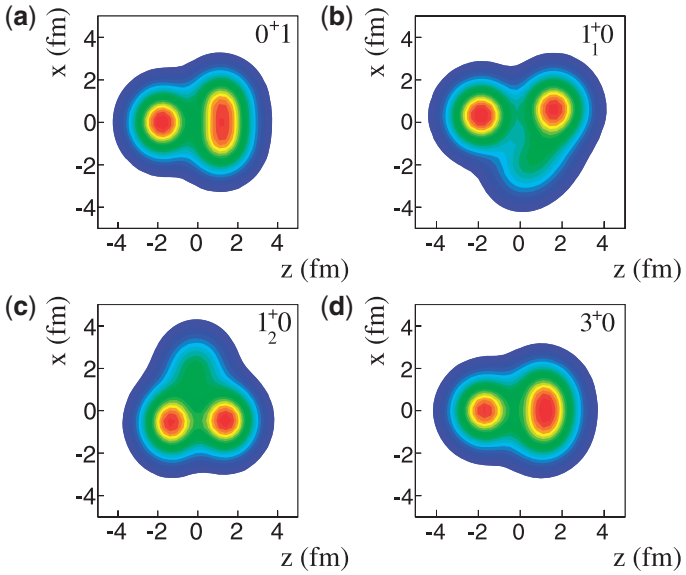

Fig. 5. Intrinsic density of the states at the minimum points in the J^π-projected energy surfaces of VAP^T. Panels (a), (b), (c), and (d) show the density distribution projected to the xz-plane of 0^+1, $1^+_1 0$, $1^+_2 0$, and 3^+0, respectively.

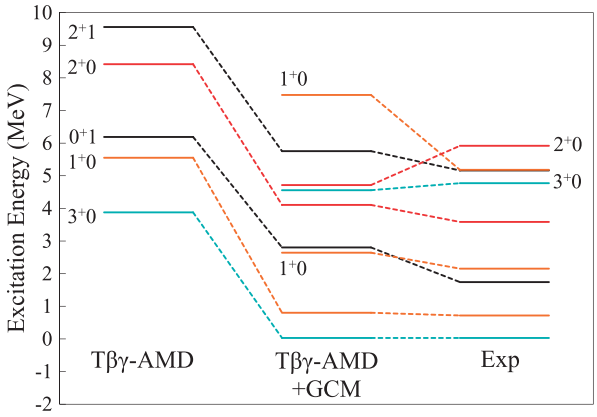

Fig. 6. Spectra of ^{10}B calculated by $T\beta\gamma$-AMD+GCM and those of the experimental data taken from Ref. [26]. The minimum energies in the J^π-projected energy surfaces of $T\beta\gamma$-AMD measured from the $3^+_1 0$ energy of $T\beta\gamma$-AMD+GCM are also shown.

The $T = 0$ and $T = 1$ energy spectra of ^{10}B obtained by the GCM calculation are shown in Fig. 6. Compared with the minimum energies of the $J^\pi T$ energy surfaces on the $\beta\gamma$-plane, about 4 MeV energy gain is obtained for the lowest $J^\pi T$ states by the superposition in the GCM calculation, mainly because of the quantum mixing of spatial and spin configurations of the *pn* pair. In particular, the $1^+_1 0$ state gains a larger energy than the $3^+_1 0$ because of the spatial motion of the *pn* pair along the plateau on the energy surface. As a result, the excitation energy of the $1^+_1 0$ state decreases in the GCM calculation. Moreover, we obtain excited $J^\pi T$ states as a result of configuration mixing as well as K-mixing in the GCM calculation. The energy spectra of the GCM calculation reasonably reproduce the experimental spectra of $T = 0$ and $T = 1$ states. Note that the relative energy between the $T = 1$ and $T = 0$ states strongly depends on the interaction parameters, B and H.

Table 1. Nuclear properties and transition strengths of ^{10}B. The calculated values obtained by $T\beta\gamma$-AMD+GCM and those obtained for the minimum energy states of the J^π-projected energy surfaces of $T\beta\gamma$-AMD in Fig. 4 are shown. The results of the AMD+VAP^J calculation in Ref. [22] are also shown. The experimental proton radii are derived from the charge radii in [27]. Other experimental data are taken from [26,28].

Observable	$T\beta\gamma$-AMD	$T\beta\gamma$-AMD+GCM	AMD+VAP^J	Exp
$\lvert E\left(3^+_1 0\right)\rvert$ (MeV)	56.5	60.4	57.7	64.75
$r_p\left(3^+_1 0\right)$ (fm)	2.3	2.4	2.33	2.28(5)
$Q\left(3^+_1 0\right)$ (e fm^2)	7.5	8.4	8.2	8.47(6)
$\mu\left(3^+_1 0\right)$ (μ_N)	1.8	1.8	1.85	1.8006
$\mu\left(1^+_1 0\right)$ (μ_N)	0.8	0.8	0.84	0.63(12)
$B\left(E2; 1^+_1 0 \to 3^+_1 0\right)$	3.0	4.0	3.6	4.14(2)
$B\left(E2; 1^+_1 0 \to 1^+_2 0\right)$	—	9.2	10.1	15.6(17)
$B\left(E2; 1^+_2 0 \to 3^+_1 0\right)$	—	2.0	1.3	1.7(2)
$B\left(M1; 0^+_1 1 \to 1^+_1 0\right)$	8.7	15.0	14.7	7.5(32)
$B\left(M1; 1^+_2 0 \to 0^+_1 1\right)$	—	0.1	0.0	0.19(2)

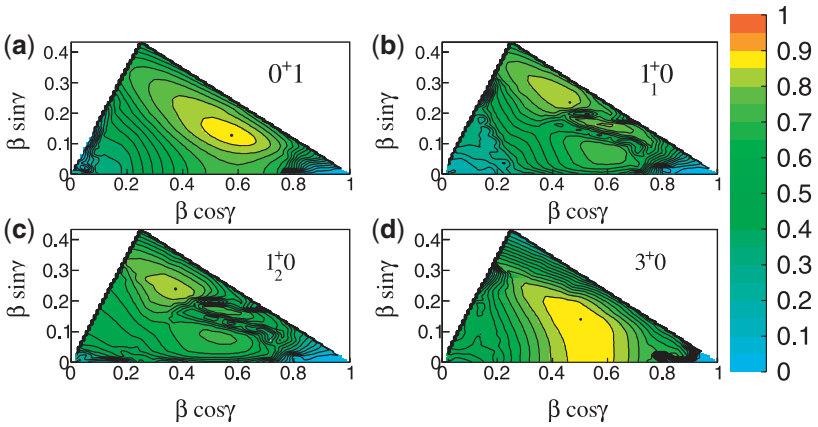

Fig. 7. Overlap amplitudes on the $\beta\gamma$-plane of ^{10}B. Panels (a), (b), (c), and (d) refer to the 0^+1, $1^+_1 0$, $1^+_2 0$, and 3^+0 states, respectively. The maximum of each surface is shown by a dot.

Table 1 shows the calculated values of nuclear properties compared with the experimental data. The present $T\beta\gamma$-AMD+GCM calculation reproduces well the ground state properties such as the point-proton radius r_p, the electric quadrupole moment Q, and the magnetic moment μ, and also describes reasonably the experimental data of $E2$ and $M1$ transition strengths.

In Fig. 7, we show the overlap amplitudes of the 0^+1, $1^+_1 0$, $1^+_2 0$, and 3^+0 states obtained by the GCM calculation with the basis wavefunctions $\Phi\left(\beta_i\gamma_i\right)$ on the $\beta\gamma$-plane. The overlap amplitudes are calculated by projection to the subspace composed of J^π-projected states, $\left\{P^T P^\pi P^J_{MK} \left|\Phi\left(\beta_i\gamma_i\right)\right\rangle\right\}_{K=-J,\ldots,J}$. For the ^{10}B$(1^+_1 0)$ and ^{10}B(0^+_1) states, the overlaps are distributed widely along the plateaus indicating the spatial development of the $T=0, S=1$ and $T=1, S=0$ pn pairs, respectively. For the ^{10}B$(3^+_1 0)$, the overlap is distributed in the small-γ region corresponding to the flat region around the energy minimum toward the $\gamma=0$ line on the $J^\pi T = 3^+0$-projected energy surface [Fig. 4(d)]. This result indicates that ^{10}B$(3^+_1 0)$ has less spatial development of the pn pair and is regarded as the almost prolately deformed state with γ fluctuation.

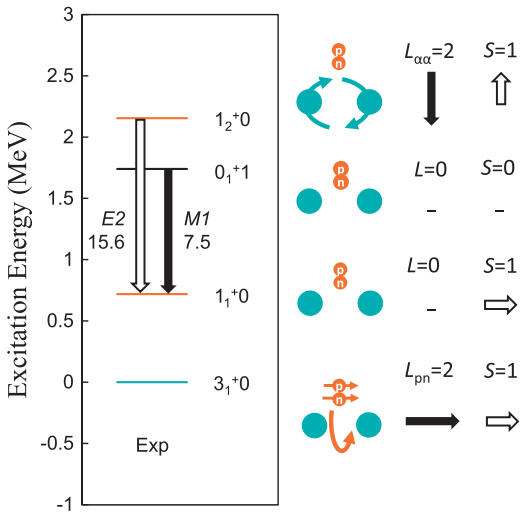

Fig. 8. Schematic figure of spin configurations of the *pn* pair and coupling with the orbital angular momentum in the low-lying states of ^{10}B. The experimental spectra are also shown. L, $L_{\alpha\alpha}$, and L_{pn} denote the total orbital angular momentum, the orbital angular momentum of the 2α core, and that of the center of mass motion of the *pn* pair. S means the intrinsic spin of the *pn* pair.

5. Discussion

In this section, we discuss the structures of the low-lying states in ^{10}B and describe the spin and spatial configurations of the *pn* pair.

As discussed previously, the $T = 0$ and $T = 1$ states of ^{10}B have dominant $S = 1$ and $S = 0$ *pn* pairs around the 2α core, respectively. The finite spin ($S = 1$) of the $T = 0$ pair couples with the orbital angular momentum L to the total angular momentum J. In the $2\alpha + pn$ structures, the orbital angular momentum (L_{pn}) for the *pn* pair motion relative to the 2α core and that ($L_{2\alpha}$) for the 2α core rotation contribute to the total orbital angular momentum L. Table 2 shows the expectation values $\langle \boldsymbol{L}^2 \rangle$ and $\langle \boldsymbol{S}^2 \rangle$ of the squared total orbital angular momentum and total spin angular momentum of the 3_1^+0, 1_1^+0, 1_2^+0, and 0_1^+1 states obtained by $T\beta\gamma$-AMD+GCM. $\langle \boldsymbol{S}^2 \rangle = 2.0$ of the $T = 0$ states indicates the almost pure $S = 1$ *pn* pair in the 3_1^+0, 1_1^+0, and 1_2^+0 states, and $\langle \boldsymbol{S}^2 \rangle = 0.3$ of the $T = 1$ state means a dominant $S = 0$ component with slight mixing of the $S = 1$ component in the 0_1^+1 state. It should be noted that the present results for $\langle \boldsymbol{L}^2 \rangle$ and $\langle \boldsymbol{S}^2 \rangle$ are almost consistent with those of the no-core shell model calculation in Ref. [29], in which analysis of the LS-coupling scheme was performed for light nuclei.

Then, the structures of the 0^+1, 3^+0, 1_1^+0, and 1_2^+0 states are understood by the $T = 0$ $S = 1$ *pn* pair and $T = 1$ $S = 0$ *pn* pair moving around the 2α core as follows. We show schematic figures of spin configurations of the *pn* pairs and their coupling with orbital angular momentum in Fig. 8. The 0^+1 state has the dominant $L = 0$ component with the $S = 0$ *pn* pair in the S-wave around the 2α core. This state is the isobaric analogue state of ^{10}Be having an $S = 0$ *nn* pair around the 2α core. The 1_1^+0 state dominantly contains the $L = 0$ component with the $S = 1$ *pn* pair in S-wave. This state is regarded as the spin partner of the 0_1^+1 state. Because of the spin-flip transition in the *pn* pair from $S = 0$ to $S = 1$, it has a strong $M1$ transition from 0_1^+1 to 1_1^+0, as shown in Table 1. The 1_2^+0 state appears from the excitation of the orbital angular momentum from $L = 0$ to $L = 2$ mainly contributed by the rotation of the 2α core ($L_{2\alpha} = 2$). The strong $E2$ transition from the 1_2^+0 state to the 1_1^+0 state (see Table 1) shows the feature of the $L_{2\alpha} = 2$ excitation in the 1_2^+0 state. The 3_1^+0 state

Table 2. The expectation values $\langle \boldsymbol{L}^2 \rangle$ and $\langle \boldsymbol{S}^2 \rangle$ of the squared total orbital angular momentum and total spin angular momentum. The values obtained by $T\beta\gamma$-AMD+GCM and those calculated for the energy minimum states of the J^π-projected energy surfaces in Fig. 4 ($T\beta\gamma$-AMD) are shown.

State	$\langle \boldsymbol{L}^2 \rangle$		$\langle \boldsymbol{S}^2 \rangle$	
	$T\beta\gamma$-AMD	$T\beta\gamma$-AMD+GCM	$T\beta\gamma$-AMD	$T\beta\gamma$-AMD+GCM
$3^+_1 0$	7.1	7.2	2.0	2.0
$1^+_1 0$	1.0	0.4	2.0	1.9
$1^+_2 0$	—	5.4	—	1.9
$0^+_1 1$	0.3	0.3	0.3	0.3

has a dominant $L = 2$ component, which is mainly contributed by the orbital angular momentum $L_{pn} = 2$ of the $S = 0$ *pn* pair. From the cluster point of view, the $S = 1$ *pn* pair aligned to $L_{pn} = 2$ feels strong spin–orbit potential from the 2α core. The strong attraction of the spin–orbit potential for the $S = 1$ *pn* pair in the *D*-wave is the origin of the level inversion in ^{10}B between the $1^+_1 0$ and $3^+_1 0$ states with *S*-wave and *D*-wave *pn* pairs, respectively, as pointed out in Ref. [22]. Note that this corresponds to the $p^2_{3/2}$ configuration in the *jj*-coupling scheme.

6. Summary and outlook

We developed a new framework of isospin-projected AMD with the $\beta\gamma$ constraint and GCM called $T\beta\gamma$-AMD+GCM for the study of $N = Z =$ odd nuclei. To test the applicability of the method we applied it to ^{10}B. The formation of the $S = 1$ and $S = 0$ *pn* pairs around the 2α core in the low-lying $T = 0$ and $T = 1$ states of ^{10}B is described in the $T\beta\gamma$-AMD+GCM calculation. The spatial development of the $T = 0$ and $T = 1$ *pn* pairs as well as the core deformation is controlled by the $\beta\gamma$ constraint in isospin-projected AMD. By superposition of the optimized wave functions on the $\beta\gamma$-plane with GCM, the spatial motion of the *pn* pair as well as the core rotation is taken into account.

The $T\beta\gamma$-AMD+GCM calculation reproduces reasonably the properties of low-lying states of ^{10}B. The structures of the lowest four states ($3^+_1 0$, $1^+_1 0$, $1^+_2 0$, and $0^+_1 1$) are understood by the angular momentum coupling of the *pn* pair internal spin (*S*), its spatial motion, and the core rotation. The $3^+_1 0$ ($1^+_1 0$) state is described by the $2\alpha + pn$ structure having the $T = 0, S = 1$ *pn* pair in the *D*-wave (*S*-wave) around the 2α core. Because of the spin–orbit attraction from the core for the $S = 1$ *pn* pair in the *D*-wave, the $3^+_1 0$ state comes down to the ground state. The $1^+_2 0$ appears from the excitation of the 2α core rotation and has the strong $E2$ transition to the $1^+_1 0$ state. The $0^+_1 1$ state, which is the isobaric analogue state of the ^{10}Be ground state, is regarded as the spin partner of the $1^+_1 0$ state, and it has the strong $M1$ transition from the $1^+_1 0$ state.

It was found that $T\beta\gamma$-AMD+GCM can describe spin configurations and spatial development of the *pn* pair in $T = 0$ and $T = 1$ states as well as the core deformation and rotation. The *pn* pair motion relative to the core and also the shape fluctuation of the deformed core are taken into account by the $\beta\gamma$ constraint with GCM. This is one of the advantages over AMD+VAP^J, which is based on the J^π-projected wave function of a single Slater determinant. It was also shown that isospin projection before the energy variation is necessary to obtain the optimum solution for each isospin state in $Z = N =$ odd nuclei, in which different isospin states almost degenerate in the low-energy region. In this study, the isospin projection operator is approximated, but we found that it is sufficient to deal with a *pn* ($T = 0, 1$) pair in the valence orbit.

The present method is expected to be useful to investigate structure with a *pn* pair around a deformed core in other $N = Z =$ odd nuclei such as ^{22}Na and ^{26}Al, in which various $J^\pi T$ states appear in low-lying spectra. In principle, in $T\beta\gamma$-AMD+GCM the existence of a *pn* pair or clusters is not *a priori* assumed. Therefore, it is applicable to general $N = Z =$ odd nuclei, and might enable us to make systematic study of *pn* pair correlations in nuclei along the $N = Z$ line.

Acknowledgements

The author would like to thank Dr Kobayashi for fruitful discussions. The computational calculations of this work were performed using the supercomputer in the Yukawa Institute for Theoretical Physics, Kyoto University. This work was supported by JSPS KAKENHI Grant Number 26400270.

References

[1] S. Frauendorf and A. O. Macchiavelli, Prog. Part. Nucl. Phys. **78**, 24 (2014).
[2] H. Wolter, A. Faessler, and P. Sauer, Nucl. Phys. A **167**, 108 (1971).
[3] A. L. Goodman, Adv. Nucl. Phys. **11**, 263 (1979).
[4] A. Gezerlis, G. F. Bertsch, and Y. L. Luo, Phys. Rev. Lett. **106**, 252502 (2011).
[5] K. Yoshida, Phys. Rev. C **90**, 031303(R) (2014).
[6] C. Qi, J. Blomqvist, T. Bäck, B. Cederwall, A. Johnson, R. J. Liotta, and R. Wyss, Phys. Rev. C **84**, 021301(R) (2011).
[7] B. Cederwall et al., Nature **469**, 68 (2011).
[8] Y. Tanimura, H. Sagawa, and K. Hagino, Prog. Theor. Exp. Phys. **2014**, 053D02 (2014).
[9] H. Sagawa, Y. Tanimura, and K. Hagino, Phys. Rev. C **87**, 034310 (2013).
[10] Y. Fujita et al., Phys. Rev. C **91**, 064316 (2015).
[11] P. Navtáril and W. E. Ormand, Phys. Rev. C **68**, 034305 (2003).
[12] P. Navtáril, V. G. Gueorguiev, J. P. Vary, W. E. Ormand, and A. Nogga, Phys. Rev. Lett. **99**, 042501 (2007).
[13] A. Ono, H. Horiuchi, T. Maruyama, and A. Onishi, Phys. Rev. Lett. **68**, 2898 (1992).
[14] Y. Kanada-En'yo, H. Horiuchi, and A. Ono, Phys. Rev. C **52**, 628 (1995).
[15] Y. Kanada-En'yo and H. Horiuchi, Prog. Theor. Phys. Suppl. **142**, 205 (2001).
[16] Y. Kanada-En'yo M. Kimura, and H. Horiuchi, C. R. Physique **4**, 497 (2003).
[17] Y. Kanada-En'yo, M. Kimura, and A. Ono, Prog. Theor. Exp. Phys. **2012**, 01A202 (2012).
[18] M. Kimura, Phys. Rev. C **69**, 044319 (2004).
[19] T. Suhara and Y. Kanada-En'yo, Prog. Theor. Phys. **123**, 303 (2010).
[20] Y. Kanada-En'yo, Phys. Rev. Lett. **81**, 5291 (1998).
[21] A. Ono, H. Horiuchi, T. Maruyama, and A. Ohnishi, Prog. Theor. Phys. **87**, 1185 (1992).
[22] Y. Kanada-En'yo, H. Morita, and F. Kobayashi, Phys. Rev. C **91**, 054323 (2015).
[23] A. B. Volkov, Nucl. Phys. **74**, 33 (1965).
[24] N. Yamaguchi, T. Kasahara, S. Nagata, and Y. Akaishi, Prog. Theor. Phys. **62**, 1018 (1979).
[25] R. Tamagaki, Prog. Theor. Phys. **39**, 91 (1968).
[26] D. R. Tilley, J. H. Kelley, J. L. Godwin, D. J. Millener, J. E. Purcell, C. G. Sheu, and H. R. Weller, Nucl. Phys. A **745**, 155 (2004).
[27] I. Angeli and K. P. Marinova, At. Data Nucl. Data Tables **99**, 69 (2013).
[28] F. Ajzenberg-Selove, Nucl. Phys. A **490**, 1 (1988).
[29] C. W. Johnson, Phys. Rev. C **91**, 034313 (2015).